

Article

# Experimental Study on the Pre-Peak Mechanical and Seepage Characteristics of Granite

Xinyan Zeng, Wancang Lin, Xinyi Chen and Qinglong Zhou \*

School of Resource and Safety, Central South University, Changsha 410083, China; 215512097@csu.edu.cn (X.Z.); wancanglin@csu.edu.cn (W.L.); 225512128@csu.edu.cn (X.C.)

\* Correspondence: zhouqinglong@csu.edu.cn

**Abstract:** The Sanshandao Gold Mine is currently in the deep mining stage. The ground pressure on the surrounding rocks is gradually becoming more considerable, and at the same time, threatened by the overlying seawater, the possibility of mine water inrush accidents is increasing. In this study, the MTS815 rock triaxial seepage test system was employed for the triaxial compression testing and stress–seepage coupled testing of granite under different confining pressures. The results show that granite’s pre-peak mechanical evolution under different confining pressures is divided into four stages (the crack closure stage, linear elasticity stage, stable crack expansion stage, and unstable crack expansion stage). With the increase in the confining pressure, the crack initiation threshold, crack damage threshold, and peak threshold gradually increased, but the closure threshold had no corresponding change. Moreover, in the loading process, the permeability curve first decreased and then increased, and the confining pressure suppressed the peak permeability of granite. Finally, based on the test results, stress sensitivity analysis was carried out, and it was found that polynomials fit the relationship between permeability and effective stress better. Granite’s permeability showed strong stress sensitivity at medium confining pressures. The stress sensitivity of the permeability of granite decreased with increasing effective stress at medium and high confining pressures, while it tended to increase at low confining pressures.

**Keywords:** granite; pre-peak mechanical characteristic; stress threshold; pre-peak seepage characteristic; permeability; stress sensitivity



**Citation:** Zeng, X.; Lin, W.; Chen, X.; Zhou, Q. Experimental Study on the Pre-Peak Mechanical and Seepage Characteristics of Granite. *Appl. Sci.* **2024**, *14*, 925. <https://doi.org/10.3390/app14020925>

Academic Editor: Tiago Miranda

Received: 2 January 2024

Revised: 17 January 2024

Accepted: 20 January 2024

Published: 22 January 2024



**Copyright:** © 2024 by the authors. Licensee MDPI, Basel, Switzerland. This article is an open access article distributed under the terms and conditions of the Creative Commons Attribution (CC BY) license (<https://creativecommons.org/licenses/by/4.0/>).

## 1. Introduction

With the increasing depletion of land-based easy-to-exploit resources, mineral resource extraction is moving in the direction of the sea. The Sanshandao Gold Mine is the first metal mine in China to engage in underground mining of coastal deposits on the continental shelf [1]. The ore body is mainly hosted in the granitic bedrock of the fault zone [2]. According to statistics, water inrush accidents related to fracture zones account for more than 80% of all water inrush accidents [3]. In agreement with the literature [4], the current mining of the Sanshandao mine is in the deep mining stage, and the hydrogeological conditions have become more complex. The mining of the ore body not only has a disturbing effect on the underground stress field but also alters its fissures, which, in turn, creates water-conducting channels and increases the possibility of water inrush accidents. In conclusion, the occurrence of a water inrush accident is a process in which the stress field and the seepage field interact and couple with each other.

The progressive failure of rocks is associated with many rock engineering problems [5]. It responds to the gradual development, expansion, and connectivity of new cracks, which can reveal the mechanical evolution characteristics of the rocks. In recent years, many scholars have conducted extensive research on the progressive failure of rocks: Wang et al. [6] studied the influence of bedding on the progressive failure process of rocks and carried out triaxial compression tests on different beddings. It was found that the pre-peak failure

process of shale was divided into an elastic stage, a stable crack propagation stage, and an unstable crack propagation stage. Xue et al. [7] found that the crack closure threshold, crack initiation threshold, and damage threshold can divide the failure process of rock samples into different stages. At the same time, the ratio of the threshold to uniaxial compressive strength can be used as an important index to predict the degree of rock failure. Nicksiar [8] proposed a new method of LSR to determine the crack initiation threshold of rock with low porosity. At the same time, it was compared with the other five strain-based methods to determine the crack initiation threshold. It was found that the former eliminated the interference of human factors. Li et al. [9] studied the influence of anisotropy on the initiation mechanism and evolution of cracks in the progressive failure process of shale and found that the ratio of the stress threshold to peak strength can provide meaningful information about the anisotropic deformation and failure mechanism of shale. Wei et al. [10] carried out uniaxial and triaxial compression tests on hard sandstone, proposed an improved crack initiation criterion to determine the crack initiation threshold of rock samples and verified the triaxial compression test data of different rock types. Xiao et al. [11] conducted conventional triaxial tests on red sandstone at different seepage pressures and found that the stress threshold decreased with increasing seepage pressure. Amann et al. [12] used the acoustic emission technique to determine the crack initiation threshold and damage threshold. It was found that the crack initiation threshold was 30% of the fracture stress and the crack damage threshold was 70% of the fracture stress. Song et al. [13] proposed a structural evolution theory based on energy evolution, microscopic characteristics, and rock burst initiation to reveal the rock's progressive failure process and rupture mechanism. Luo et al. [14] explored the progressive rock failure mechanism from the perspective of energy accumulation and dissipation and found that the eigenvalue of the elastic strain energy increased quasi-linearly with an increase in the confining pressure. The eigenvalue of the dissipation energy steadily increased with the increase in the confining pressure. The above researchers have conducted many positive investigations on the progressive failure analysis of rocks, but there are few reports on the pre-peak progressive failure analysis of rocks.

With the increasing depletion of land-based mineral resources, the exploitation of marine mineral resources has become a new direction of development. Compared with the exploitation of land-based mineral resources, due to the threat of the underlying seawater, the exploitation of marine mineral resources is very complex [15]. In recent years, stress–permeability coupling has also gradually become prevalent, and many researchers have conducted a lot of research in the field of fluid–solid coupling. Jia et al. [16] found that with an increase in effective stress, the permeability and porosity of granite decrease gradually. The relationship between effective stress and permeability can be described via the exponential and power law. Chen et al. [17] showed that the permeability with stress differences showed four stages: slow decline, smooth development, slow increase, and rapid increase. Wang et al. [18] carried out stress–seepage coupling tests under different pore pressures and found that the permeability of granite increased with the increase in the initial pressure difference. Souley et al. [19] and Oda et al. [20] studied the evolution of the permeability of brittle intact rocks during conventional triaxial compression tests, revealing the coupling mechanism between rock permeability and damage processes. The effects of seepage pressure, confining pressure, and rock microstructure on permeability evolution have been investigated [17,21,22]. Some tests have shown that deviatoric stress leads to the development and expansion of cracks in brittle rocks, leading to a significant increase in permeability [19,23]. Meng et al. [24] conducted solid–flow coupling tests on calcareous sedimentary rocks and proposed a corresponding weakening mechanism based on the law of the evolutionary process of permeability and microstructures. Xiao et al. [11] found that the peak permeability of sandstone lagged behind the peak stress under different seepage pressures and showed a sudden jump near the peak stress. Most of the previous studies have focused on the effects of seepage pressure, confining pressure, and microstructure

on rock permeability, and little has been reported on the evolution of pre-peak stress–permeability, which is of engineering concern.

In summary, there are few studies on granite’s mechanical and seepage pre-peak characteristics. The MTS815 rock triaxial seepage test system was employed to test the triaxial compression–seepage conditions under different confining pressures to reveal granite’s mechanical and seepage pre-peak characteristics. Based on the test results, stress sensitivity analyses were carried out to show the permeability stress sensitivity of granite under different confining pressures. The results of this study will be helpful for the establishment of a coupled flow–solid model for the safe mining of bedrock deposits on the seabed of Sanshandao and provide corresponding data support.

## 2. Test Methods and Principles

### 2.1. Stress–Seepage Coupling Test

Considering granite as a low-permeability rock, the transient method was used in the MTS815 rock triaxial seepage test system to determine the permeability of the rock samples, as shown in Figure 1. During the seepage test, the change in the seepage pressure difference  $\Delta P$  was the only indicator of the permeability of the rock [24,25]. Combined with the data automatically collected with the computer in the test, the following formulation was used to calculate the permeability of the rock:

$$K = \frac{1}{5A} \sum_{I=1}^A m \lg [\Delta P(I-1)/\Delta P(I)] \quad (1)$$

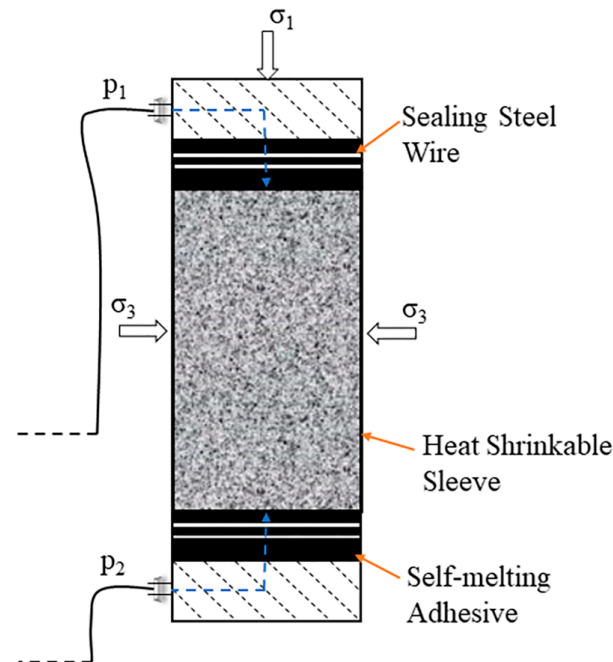
where  $A$  is the number of data collection lines;  $m = 526 \times 10^{-6}$  is the value of the test parameter [26,27]; and  $\Delta P(I-1)$  and  $\Delta P(I)$  are the seepage pressure differences in rows  $I-1$  and  $I$ , respectively.  $K$  is the permeability ( $\text{m}^2$ ) ( $1 \text{ Darcy} = 0.986923 \times 10^{-12} \text{ m}^2$ ).



Figure 1. Rock triaxial seepage test system.

The working principle diagram of the test is shown in Figure 2.  $\sigma_1$ ,  $\sigma_3$ ,  $P_1$ ,  $P_2$ , and  $\Delta P$  are the stress pressure, confining pressure, the water pressure on the specimen, the water pressure under the specimen, and the water pressure difference, respectively. The method

of the stress–seepage coupling test was to apply a certain confining pressure  $\sigma_3$ , an axial pressure  $\sigma_1$ , and the water pressure on the specimen  $P_1$ , and then apply the water pressure under the specimen  $P_2$ , resulting in the formation of a seepage pressure difference between the two ends of the specimen, where  $\Delta P = P_1 - P_2$ .



**Figure 2.** Schematic diagram of stress–seepage loading of rock samples.

#### Test Procedure

(1) The rock sample was wrapped in a heat-shrinkable tube and sealed with a blower. (2) The confining pressure was applied with a loading rate of 0.5 MPa/s until the confining pressure reached the set value. (3) Then, the axial pressure was applied with a loading rate of 0.2 KN/s until the axial pressure reached the set value. (4) A pore loading system was used to apply the water pressure on the granite  $P_1$  and the water pressure under the specimen  $P_2$ , respectively, at a loading rate of 0.2 MPa/s up to a set value, resulting in an initial water pressure difference,  $\Delta P$ . To avoid water leakage from the side wall of the heat-shrinkable tube, the value of the confining pressure was more than 1 MPa, which was larger than the water pressure during the test. (5) The value of the confining pressure was changed, and steps (1)–(4) were repeated until all rock samples were tested. The specimen test conditions are presented in Table 1.

**Table 1.** The test conditions of the specimens.

Specimen Number	$\sigma_3$ /MPa	$P_1$ /MPa	$P_2$ /MPa	$\Delta P$ /MPa
A00	5	4	1	3
B00	10	9	1	8
C00	20	18	3	15

#### 2.2. Triaxial Compression Test

##### Test Procedure

(1) The rock sample was wrapped in a heat-shrinkable tube and sealed with a blower. (2) Axial and circular strain meters were installed on the specimen to monitor the changes in the axial and radial strains during loading. (3) The confining pressure (5 MPa, 10 MPa, and 20 MPa) was applied at a loading rate of 0.5 MPa/s until the confining pressure reached the set value. (4) The axial pressure was applied at a 0.12 mm/min loading rate. The value of

the confining pressure was changed, and steps (1)–(4) were repeated until all rock samples were tested, as shown in Figure 3.

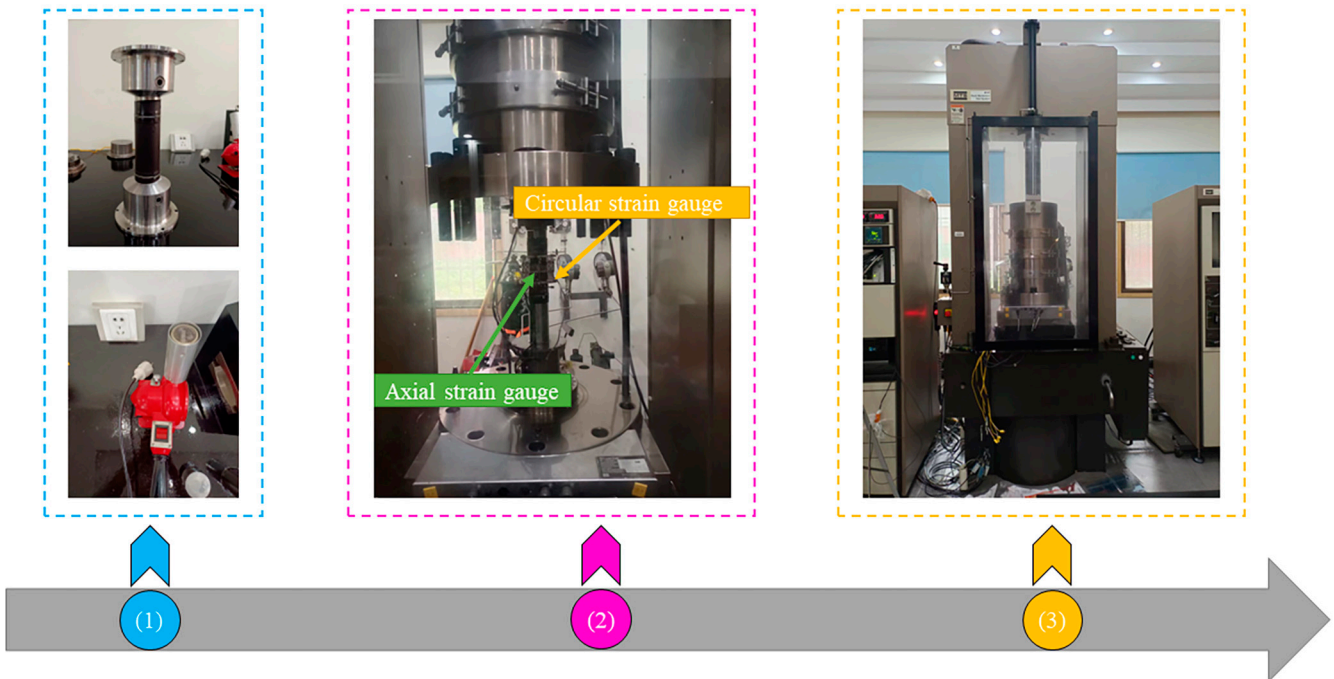


Figure 3. Flow chart of granite conventional triaxial test.

### 3. Analysis of Test Results

#### 3.1. Mechanical Characteristics

##### 3.1.1. Pre-Peak Progressive Failure Analysis

In the loading process, the rocks showed different mechanical characteristics at different stress stages. According to the deformation of the rocks and the development of cracks, the concept of a stress threshold was introduced to characterize the stress–strain process of the rocks before the peak into a gradual failure process and to analyze the change rule of the rock stress threshold, which is of great significance for monitoring the stability of the surrounding rock in seabed bedrock mining.

The characteristic thresholds in the pre-peak stress–strain process contain a crack closure threshold  $\sigma_{cc}$ , crack initiation threshold  $\sigma_{ci}$ , crack damage threshold  $\sigma_{cd}$ , and peak strength  $\sigma_p$  [28,29]. The pre-peak stress–strain process in rocks can be divided into four stages based on the stress threshold: (1) the crack closure stage (OA), (2) the linear elasticity stage (AB), (3) the stable crack expansion stage (BC), and (4) the unstable crack expansion stage (CD), as shown in Figure 4.

A lot of research has been conducted on the determination of stress thresholds. Eberhardt et al. [30] used acoustic emission techniques to identify the crack initiation strength ( $\sigma_{ci}$ ) and crack damage strength ( $\sigma_{cd}$ ) and found that the number of acoustic emission events captured starts to increase when the stress reaches  $\sigma_{ci}$ . However, determining other stress thresholds is more ambiguous due to noise in the acquisition environment. By observing the stress–volumetric strain curve, it was determined that the turning point of the curve is the crack damage strength  $\sigma_{cd}$ . This method can determine the  $\sigma_{cd}$  more intuitively, but it cannot accurately identify the  $\sigma_{ci}$  [31]. Therefore, the crack initiation strength ( $\sigma_{ci}$ ) is determined with the help of the crack volumetric strain, and the relevant formulation is given as follows:

$$\left. \begin{aligned} \varepsilon_v &= \varepsilon_1 + 2\varepsilon_3 \\ \varepsilon_{cv} &= \varepsilon_v - \frac{(1-2\mu)(\sigma_1 - \sigma_3)}{E} \end{aligned} \right\} \quad (2)$$

where  $\epsilon_1$ ,  $\epsilon_3$ ,  $\epsilon_v$ , and  $\epsilon_{cv}$  are the axial strain, radial strain, volumetric strain, and crack volumetric strain, respectively, where  $E$  and  $\mu$  are the modulus of elasticity and Poisson's ratio, respectively.

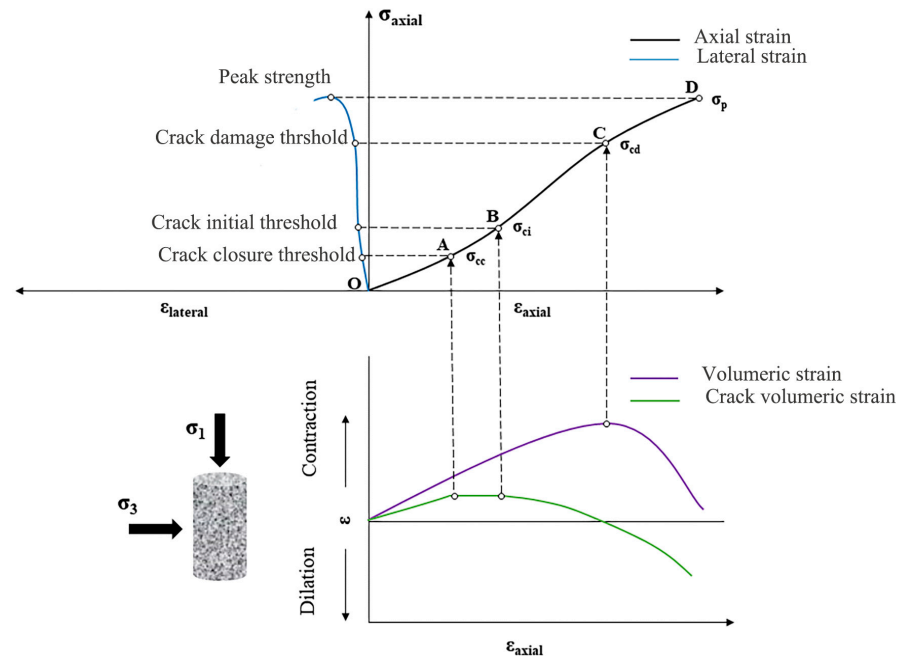


Figure 4. Schematic diagram of progressive failure process in rocks.

Considering that rock samples have greater randomness during the transition from the crack closure stage to the elasticity stage, there will be a significant error if the stress–strain curve is used to determine the crack closure strength [11]. Therefore, the axial strain difference curve was used to determine the crack closure strength, as shown in Figure 5, and its calculation formula [11] is as follows:

$$\Delta\epsilon_1 = \epsilon_1 - \frac{\sigma_1 - \sigma_3}{\sigma_{cd}} \epsilon_{cd} \tag{3}$$

where  $\Delta\epsilon_1$  and  $\epsilon_{cd}$  are the axial strain difference and the axial strain corresponding to the crack damage strength ( $\sigma_{cd}$ ).

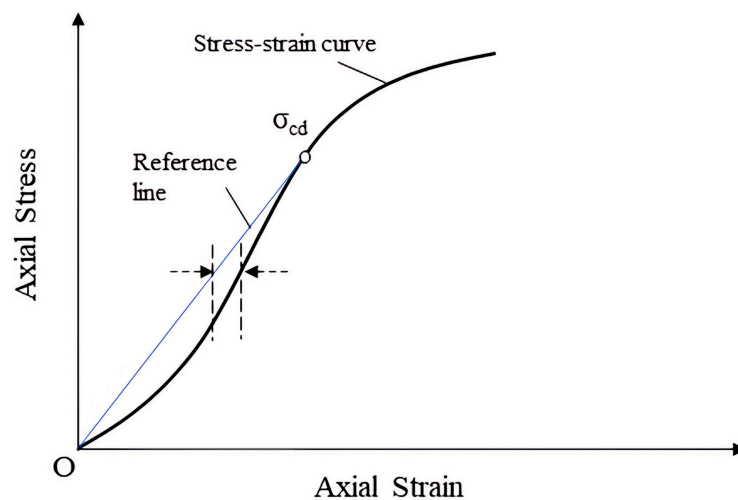


Figure 5. Determination of axial strain difference using stress–strain curve.

According to the axial strain difference calculated using the above formulation, the axial strain difference–stress curve can be plotted, as shown in Figure 6. The stress value corresponding to the peak of the curve is the crack closure strength ( $\sigma_{cc}$ ). Stress–volumetric strain curves, the crack volumetric strain, the axial strain difference, and stress–strain curves were used to determine the crack damage strength ( $\sigma_{cd}$ ), crack initiation strength ( $\sigma_{ci}$ ), crack closure strength ( $\sigma_{cc}$ ), and peak strength ( $\sigma_p$ ), respectively, of the rock during progressive rock failure under different confining pressures. The results are plotted in Figure 7. By observing Figure 7, it is found that the crack initiation strength ( $\sigma_{ci}$ ), crack damage strength ( $\sigma_{cd}$ ), and peak strength ( $\sigma_p$ ) are positively correlated with the confining pressure, but the confining pressure has no effect on the crack closure strength ( $\sigma_{cc}$ ). As a dense rock, many primary cracks are in a high-degree-of-closure state in granite. It can be concluded from Table 2 that the ratio of the crack initiation strength to peak strength at different confining pressures ranges from 0.35 to 0.37. According to the researchers’ studies in [32–34] on the cracking strength of brittle rocks, it was found that the ratio of the crack initiation strength to the peak strength is between 0.3 and 0.5. The ratio of the rock damage strength to the peak strength is in the range of 0.37 to 0.46 in this study, much lower than the range of 0.7 to 0.85 reported in the relevant literature [35]. The reason is that granite, as a dense rock, needs longer accumulation in the unstable crack expansion stage from the damage threshold to the peak strength.

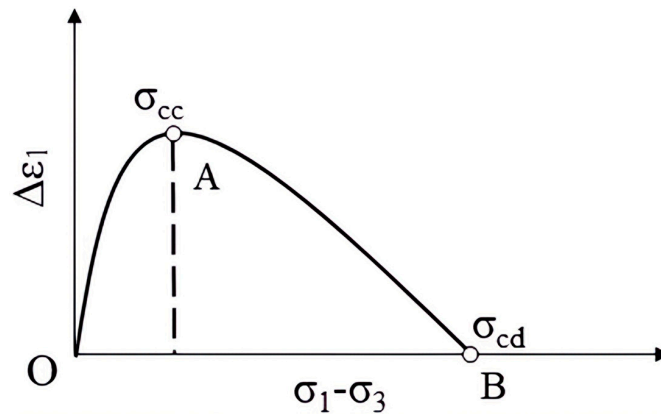


Figure 6. Stress–axial strain difference curve.

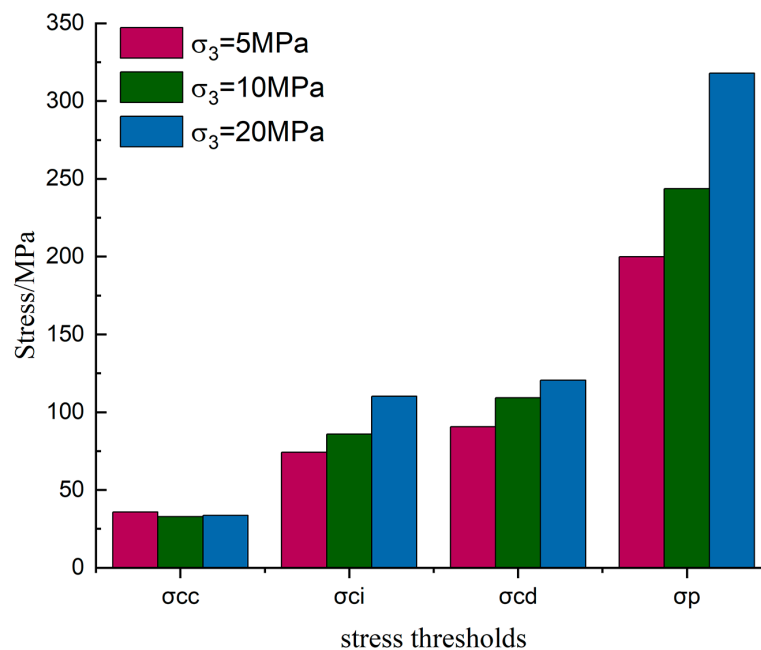


Figure 7. Stress threshold under three confining pressures.

**Table 2.** Stresses and stress ratios of granite under three confining pressures.

$\sigma_3$ (MPa)	$\sigma_{ci}$ (MPa)	$\sigma_{ci}/\sigma_p$ (%)	$\sigma_{cd}$ (MPa)	$\sigma_{cd}/\sigma_p$ (%)	$\sigma_p$ (MPa)
5	74.26	37.16	90.58	45.33	199.85
10	85.87	35.23	109.28	44.84	243.74
20	110.27	34.68	120.58	37.92	317.97

### 3.1.2. Deformation Characteristics

According to the stress threshold, the corresponding stress–strain curve can be divided into four parts: the crack closure stage I, linear elasticity stage II, stable crack expansion stage III, and unstable crack expansion stage IV, as shown in Figure 8. To better demonstrate the results, the stress–volumetric strain curve is divided into two parts, and the relevant points are interpreted in Table 3.

**Table 3.** Volumetric strain curve of each point interpretation summary table.

$\sigma_3$ (MPa)	$\sigma_{cc}$	$\sigma_{ci}$	$\sigma_{cd}$	$\sigma_p$
5	a	b	c	d
10	a'	b'	c'	d'
20	a''	b''	c''	d''

The characteristics of each deformation stage are analyzed as follows.

**Crack closure stage I:** As shown in Figure 8, it is found that the stress–strain curve and the stress–volumetric strain curve are concave and highly coincident during the crack closure stage, indicating that the rock volume gradually becomes dense when the confining pressures and axial pressures start to act on the rock samples, and only longitudinal cracks occur in response. The primary cracks in the rock samples are closed until the crack closure strength ( $\sigma_{cc}$ ).

**Linear elastic stage II:** The stress–strain curve of the rock samples shows a linear trend until the crack initiation strength ( $\sigma_{ci}$ ), which reflects the internal deformation of the rock samples as elastic deformation during the gradual increase in axial stress. Observing the volumetric strain curve, the volume of the rock samples is found to be in compression, and the primary crack continues to be closed.

**Stable crack expansion III:** As shown in Figure 8, when the axial stress starts to exceed the crack initiation strength ( $\sigma_{ci}$ ), it is found that there is no significant change in the volumetric strain, and the crack stability development stage is short. Martin [36] suggests that only secondary cracks occur parallel to the load direction change in this stage.

**Unstable crack expansion IV:** This is the final stage of the progressive failure process, the unstable expansion stage of cracks. According to Figure 8, it can be found that when the stress in the rock specimen exceeds the crack damage strength, the direction of the volumetric strain is deflected from positive to negative. This indicates that the volume of the rock sample is transformed from compaction to expansion, and a large number of secondary transverse and vertical cracks are developed in the inner part of the rock sample, and the process lasts until the peak stress ( $\sigma_p$ ).

### 3.2. Analysis of Seepage Evolution

Rock permeability is essential in determining the occurrence of water inrush in seabed mining engineering. Many factors affect permeability, including stress, seepage pressure, and confining pressure. Evidently, these factors affect the permeability characteristics of a rock by altering its cracks. In this section, the results of the mechanical characteristics are combined during the progressive failure of the granite in the previous section to reveal the pre-peak evolution of the permeability of the granite.

### The Pre-Peak Evolution Characteristics of Permeability

The permeability of the granite was calculated according to Equation (1), and the permeability pre-peak evolution curves under different confining pressures were plotted, as shown in Figure 9.

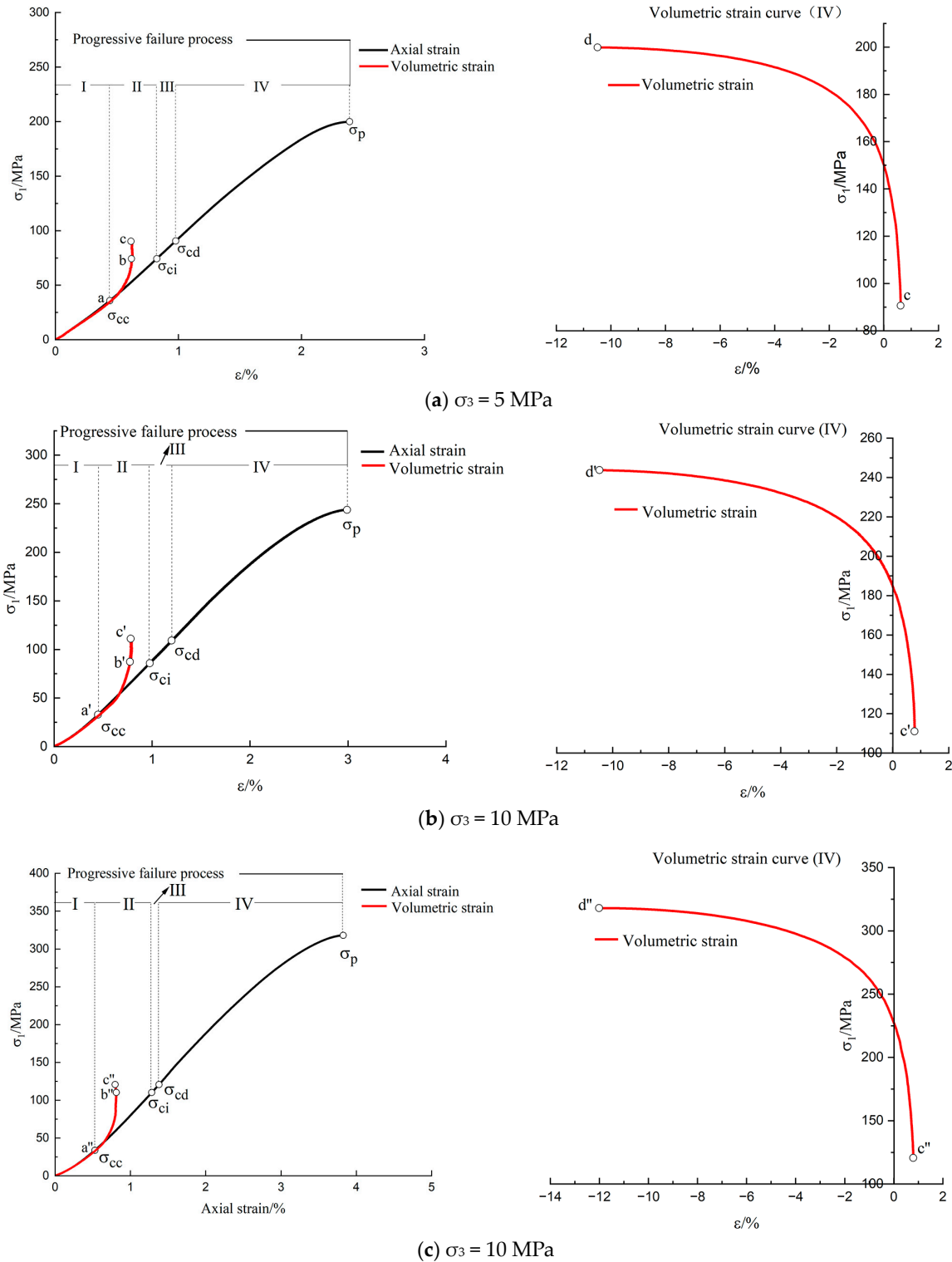
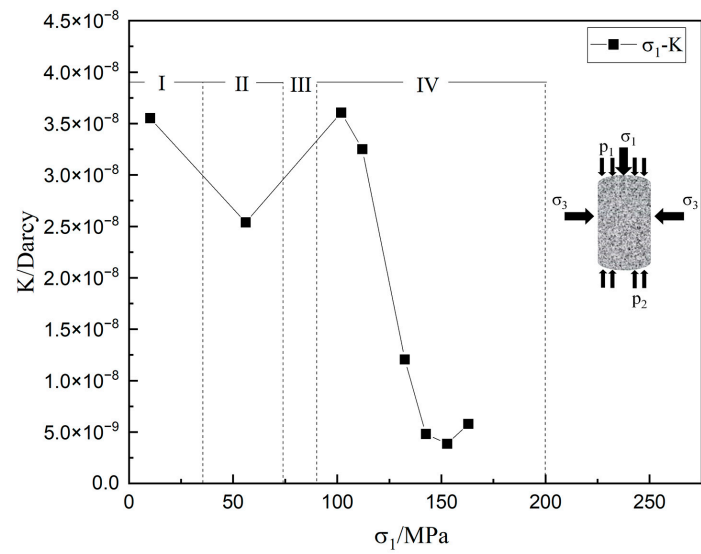
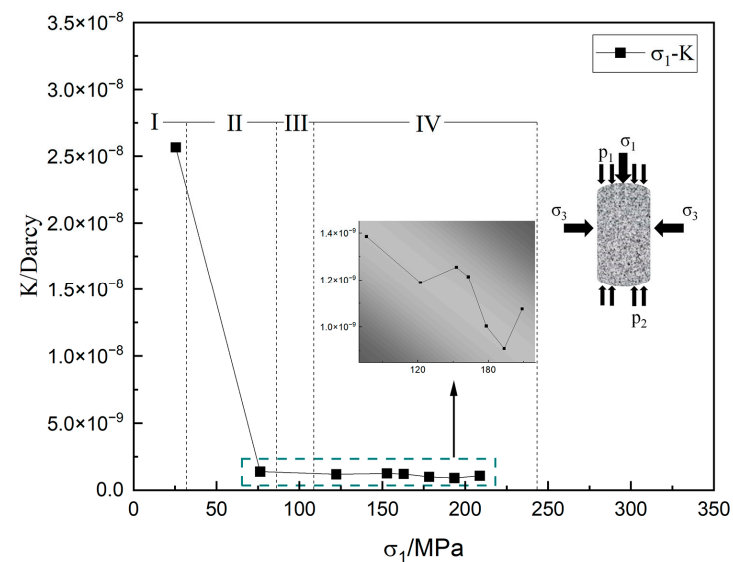


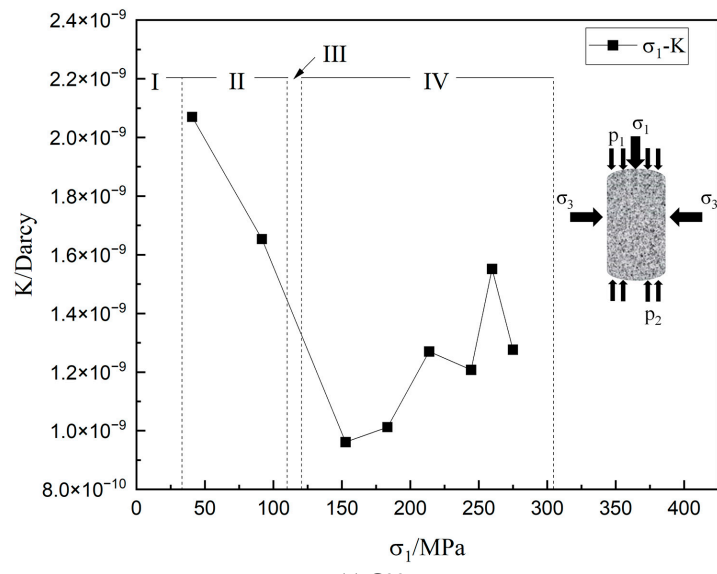
Figure 8. The volumetric curves of rock under different confining pressures.



(a) A00



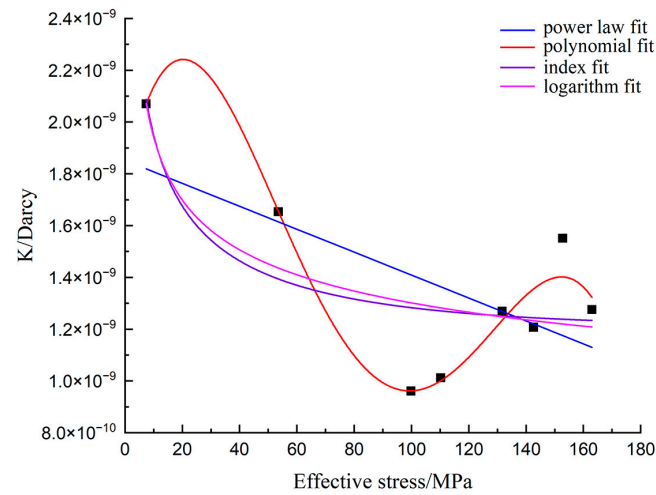
(b) B00



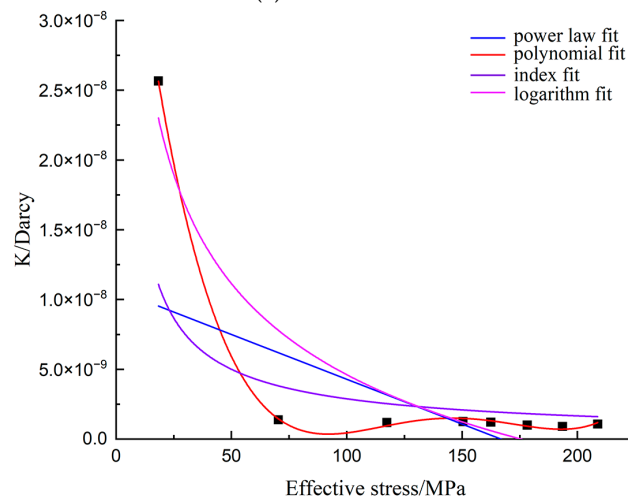
(c) C00

Figure 9. Evolution process of rock permeability in pre-peak process.

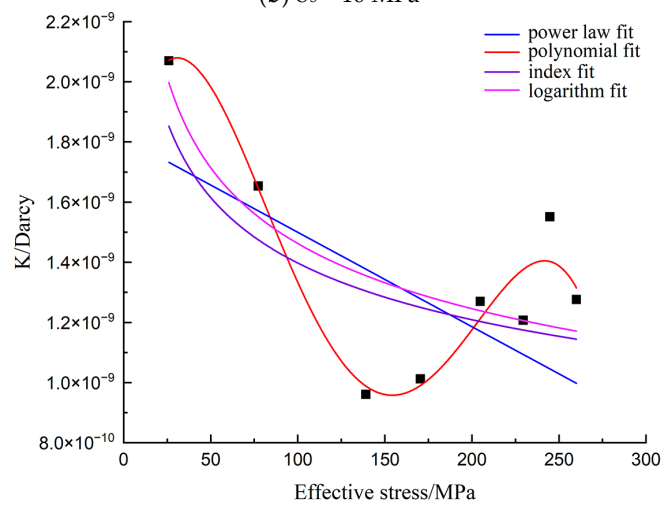
It should be noted that the four parts, I, II, III, and IV, divided in Figure 10 correspond to the crack closure stage (I), linear elasticity stage (II), stable crack expansion stage (III), and unstable crack expansion stage (IV), respectively. No stress point is set in this part, considering that the stable crack expansion stage (III) is shorter in the whole progressive failure process.



(a)  $\sigma_3 = 5 \text{ MPa}$



(b)  $\sigma_3 = 10 \text{ MPa}$



(c)  $\sigma_3 = 20 \text{ MPa}$

Figure 10. Permeability and effective stress curves.

According to Figure 9, The initial permeability of the granite at confining pressures of 5 MPa, 10 MPa, and 20 MPa were  $3.55 \times 10^{-8}$  Darcy,  $2.57 \times 10^{-8}$  Darcy, and  $2.07 \times 10^{-9}$  Darcy respectively. The initial permeability of the granite under the different confining pressures was the maximum throughout the loading process. It was found that the initial permeability of the granite gradually decreased with the increase in the confining pressure. Previous researchers have also concluded the same negative correlation between the permeability of rock samples and the confining pressure [37]. It is noteworthy that although the difference between the three levels of confining pressures was two times, the permeability values of the rock samples at 5 MPa and 10 MPa were in the same order of magnitude. In contrast, the difference between the rock samples at 20 MPa and those at 10 MPa was by one order of magnitude. The final permeability of the granite at the confining pressures of 5 MPa, 10 MPa, and 20 MPa were  $5.80 \times 10^{-9}$  Darcy,  $1.08 \times 10^{-9}$  Darcy, and  $1.28 \times 10^{-9}$  Darcy, respectively. The final permeability of the granite under different confining pressures was the minimum throughout the loading process. Interestingly, the final permeability values of the granite at 5 MPa, 10 MPa, and 20 MPa were in the same order of magnitude. Furthermore, comparing the initial permeability and final permeability of the granite under different confining pressures, it was found that both were one order of magnitude different. Therefore, the axial pressure and confining pressure were key to the decrease in the permeability. By observing Figure 9, it can be concluded that when the progressive failure process of the rock samples was in stage I, with the increase in the axial pressure, the permeability of the granite as a whole showed a decreasing trend. The cracks gradually closed at this stage, and the seepage channel slowly shrank. When the axial stress crossed the crack closure threshold ( $\sigma_{cc}$ ) and entered the linear elasticity stage (II), the closure of the internal pore cracks in the rock was complete, and the seepage channels were barren, leading to further attenuation of the permeability of the rock samples. It can be observed in Figure 9 that when the axial stress crossed the crack initiation threshold ( $\sigma_{ci}$ ) and entered into the stable crack expansion stage (III) and the unstable crack expansion stage (IV), the permeability of the granite rose. This indicates that secondary crack expansion was occurring within the sample and that the width of the seepage channels was expanding and increasing in number, resulting in the gradual recovery of the permeability of the granite. According to Figure 9, it can be found that the limitation of the permeability of rock samples by the pressure was quite critical. Zheng et al. [38] suggested that this is because the confining pressure acts to consolidate the pore and fissure pressures within the rock sample.

### 3.3. Effective Stress Analysis under Stress–Seepage Coupling

The effective stress principle is essential in stress–seepage field coupling [39]. A great deal of research has been conducted on this: Terzaghi [40] first proposed the concept of effective stress to describe the geotechnical medium via the coupling of external stress and pore water pressure. The formulation is as follows:

$$\sigma' = \sigma - p \quad (4)$$

where  $\sigma$  is the stress acting on the entire geotechnical medium,  $\sigma'$  is the stress acting on the particles of the geotechnical medium, and  $p$  is the fluid pressure between particles. The formulation is widely used in the field of geotechnical solid–flow coupling. Researchers have extended the formulation with further improvements: Biot [41] introduced an effective stress factor  $\alpha$ , which corrects the equation as follows:

$$\sigma' = \sigma - \alpha p \quad (5)$$

A big controversy exists for the effective stress coefficient  $\alpha$  value. The former also proposed a number of calculation methods. The researchers of [42] consider the effective stress factor  $\alpha$  to be equal to the porosity of the porous medium  $\varphi$ . Geertsma [43] and Skempton [44] proposed that the effective stress coefficient is related to the equivalent bulk

modulus ( $K$ ) and grain bulk modulus ( $K_s$ ) of the porous medium. The literature indicates that the effective stress coefficient does not directly depend on the porosity  $\varphi$ , and after rigorous formulation derivation and experimental validation, the following expression is obtained:

$$\alpha = 1 - K/K_s \quad (6)$$

In this paper, the volumetric modulus method proposed in the literature [45] was applied. Based on the known volumetric modulus of the rock and the equivalent volumetric modulus of the fractured rock mass, combined with the effective stress coefficients in Equation (6) and substituted into Equation (5) to derive the effective stresses, the curves between the permeability and the effective stresses are plotted in Figure 10.

Many researchers have carried out many experiments and studies to investigate the relationship between permeability and effective stress in porous media and have put forward different views and modeling relationships.

The literature [40] suggests that an exponential model can be used to describe the relationship between permeability and effective stress in porous rocks:

$$K = K_0 e^{-\beta P_c} \quad (7)$$

where  $K$  is the permeability of the porous rock,  $K_0$  is the initial permeability of the porous rock,  $\beta$  is the regression coefficient, and  $P_c$  is the effective stress acting on the porous rock.

Civan et al. [46] and Ghabezloo et al. [47] used a power law relationship to characterize the permeability of porous rocks as a function of the confining pressure:

$$K = A(\sigma_c) - B + C \quad (8)$$

where  $A$ ,  $B$ , and  $C$  are the regression coefficients, and  $\sigma_c$  is the confining pressure.

Meng et al. [48] found that the relationship between permeability and confining pressure for cohesive sandstones can be expressed as a polynomial:

$$K = a\sigma_c^2 + b\sigma_c + C \quad (9)$$

where  $a$ ,  $b$ , and  $c$  are the regression coefficients.

Xiao et al. [49] proposed the use of a logarithmic model to characterize the relationship between permeability and effective stress:

$$(K/K_{ref})^{1/3} = 1 - \text{Sin}(\sigma_{eff}/\sigma_{eff0}) \quad (10)$$

where  $\sigma_{eff}$  and  $K_{ref}$  are the initial effective stress and corresponding initial permeability, respectively, and  $\sigma_{eff}$  and  $K$  are the effective stress and related permeability, respectively. The literature [50] gives  $s = \sqrt{2}h/\alpha_{ref}$  via the derivation of the formula, where  $h$  is the height of the convex body on the microcracks.

Combining the data obtained from the tests and the bulk modulus method described in the previous section, the permeability was calculated and plotted against the effective stresses. To investigate the relationship between permeability and effective stress, the test data were fitted using the three types of appropriate equations described above, and the accuracies of the three fitting equations are summarized in Table 4. Combined with Table 4 and Figure 10, the cubic polynomial better defines the relationship between permeability and effective stress in terms of fitting accuracy.

### 3.4. Stress Sensitivity under Different Confining Pressures

In order to study the coupling mechanism of stress and seepage fields in granite during the seepage process, the stress sensitivity under different confining pressures was

investigated. In this paper, the proposed stress sensitivity factor [51] formulation was used to evaluate the stress sensitivity of granite as follows:

$$S_s = \frac{1 - (K/K_0)^{1/3}}{\lg(\sigma_{eff}/\sigma_{eff0})} \tag{11}$$

where  $S_s$  is the stress sensitivity factor,  $\sigma_{eff}$  is the effective stress,  $\sigma_{eff0}$  is the initial effective stress,  $K_0$  is the permeability corresponding to  $\sigma_{eff}$ , and  $K$  is the permeability corresponding to  $\sigma_{eff0}$ .

**Table 4.** Three kinds of relationship fitting effects summary.

$\sigma_3$ (MPa)	Equation	R <sup>2</sup>	Equation	R <sup>2</sup>	Equation	R <sup>2</sup>	Equation	R <sup>2</sup>
5	Polynomial fit	0.94932	Logarithmic fit	0.62738	Index fit	0.64015	Power fit	0.4146
10		0.99965		0.88102		0.66066		0.42554
20		0.93995		0.58227		0.85959		0.37178

According to Equation (11), the effective stress sensitivity coefficients for the effective stresses under different confining pressures curves are plotted in Figure 11. Combined with the stress sensitivity evaluation criteria proposed in the literature [49], as shown in Table 5, it was concluded that at a confining pressure of 10 MPa, the effective stress sensitivity coefficients were all greater than 0.4. It shows strong stress sensitivity, indicating that the permeability of the rock samples was greatly affected by the effective stress. The effective stress coefficients at 10 MPa and 20 MPa were in the range of 0 to 0.4, showing general stress sensitivity, indicating that the permeability of the rock samples was less affected by the effective stress.

**Table 5.** Stress sensitivity evaluation criteria based on sensitivity coefficient [49].

Stress Sensitivity Coefficient	$S_s < 0.25$	$0.25 \leq S_s \leq 0.4$	$0.4 < S_s$
Sensitivity degree	Weak	Medium	Strong

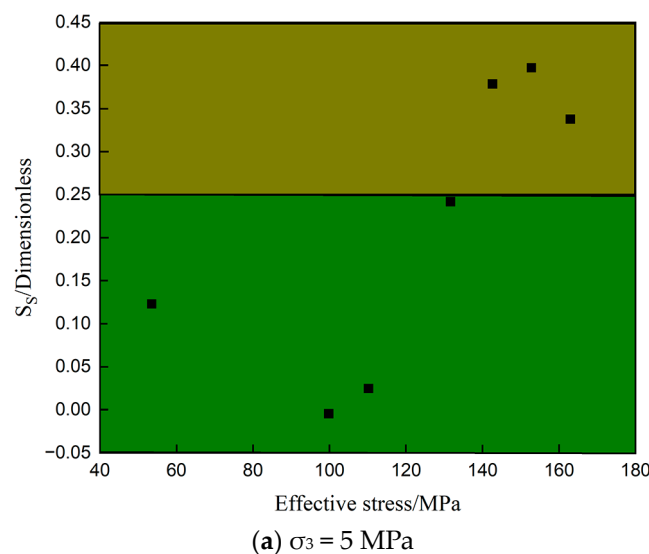


**Figure 11.** Cont.

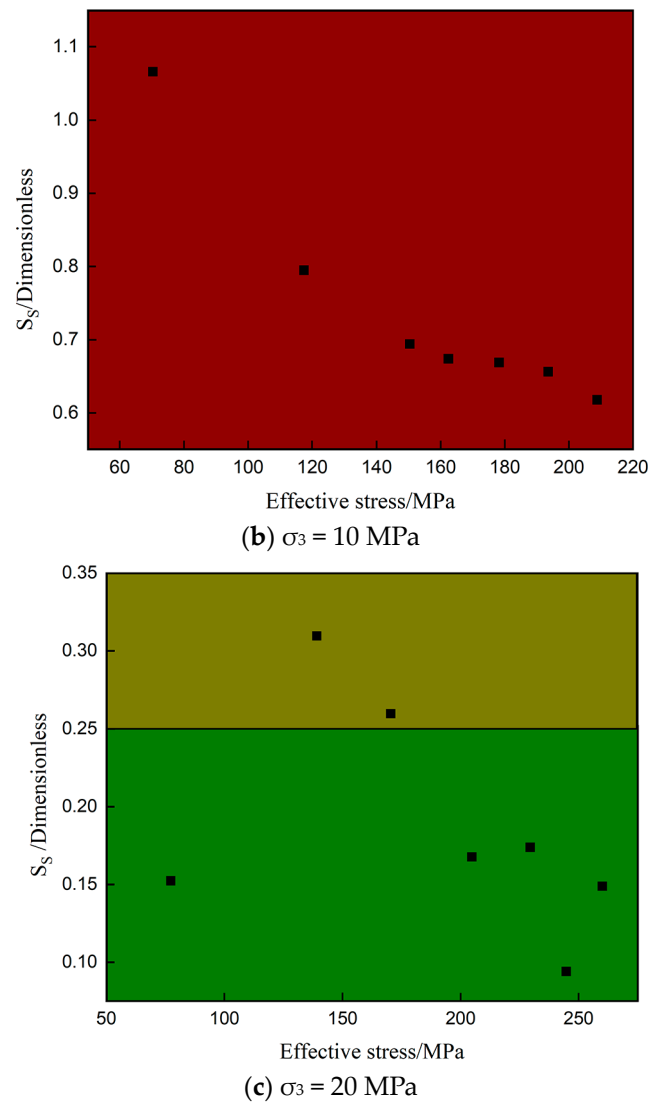


**Figure 11.** Effective stress and effective stress sensitivity coefficient under different confining pressures.

#### 4. Conclusions

In this paper, triaxial compression tests and stress–permeability coupling tests were carried out on granite to analyze the evolution laws of characteristic thresholds, deformation, and permeability in the progressive failure process of granite under different confining pressures, in addition to calculating the effective stresses of the granite under different confining pressures and carrying out the evaluation of the sensitivity of the effective stresses. The main conclusions are as follows:

1. The closure threshold, crack initiation threshold, damage threshold, and peak strength divide the evolution process of granite's pre-peak mechanical characteristics into a crack closure stage, linear elasticity stage, stable crack expansion stage, and unstable crack expansion stage. The confining pressure is positively correlated with the closure threshold, peak strength, and damage threshold.
2. In the evolution of the pre-peak permeability characteristics of granite, when the confining pressure is certain, the permeability decreases and then increases with the increase in axial stress, which is more in line with the four phases of the crack change in the progressive damage analysis. The confining pressure is negatively correlated with the peak permeability of granite. Especially, the peak permeability at a high confining pressure differs by one order of magnitude from the peak permeability at a medium confining pressure.

3. The polynomial model can better fit the relationship between effective stress and the permeability of granite. The effective stress sensitivity coefficients of granite are differently reflected at different confining pressures. At a medium confining pressure, the permeability of granite is more affected by the effective stress, while at low and high confining pressures, the effective stress has less effect on the permeability of granite. At medium and high confining pressures, with the increase in the effective stress, the stress sensitivity of the permeability of granite gradually tends to diminish, while at a low confining pressure, the trend is to increase.

Based on previous research, the closure threshold, crack initiation threshold, and damage threshold of granite were determined with the axial strain difference, crack volumetric strain curve, and volumetric strain curve, and the evolution law of progressive failure of granite under different confining pressures was obtained. The evolution law of the permeability of granite with stress under different confining pressures was obtained by combining progressive failure analysis with stress–seepage coupling analysis. The stress sensitivity analysis of granite permeability under different confining pressures was carried out, and the relationship between effective stress and permeability and the stress sensitivity coefficient of granite permeability under constant confining pressure was obtained.

The bedrock of submarine deposits is a complex hydrogeological environment. There are some shortcomings in the design of this experiment, and the hydrological environment of its occurrence was not fully reflected. The stress–seepage coupling direction of granite after corrosion can be further explored.

**Author Contributions:** Conceptualization, Q.Z.; Methodology, X.Z., W.L. and Q.Z.; Software, X.Z. and X.C.; Validation, X.Z.; Data curation, Q.Z.; Writing—original draft, X.Z., W.L. and X.C.; Writing—review & editing, Q.Z.; Visualization, W.L. All authors have read and agreed to the published version of the manuscript.

**Funding:** The authors are grateful for the financial support from the National Natural Science Foundation of China (grant no. 52004332).

**Institutional Review Board Statement:** Not applicable.

**Informed Consent Statement:** Not applicable.

**Data Availability Statement:** Data is contained within the article.

**Conflicts of Interest:** The authors declare no conflict of interest.

## References

1. Hu, F.F.; Fan, H.R.; Jiang, X.H.; Li, X.C.; Yang, K.F.; Mernagh, T. Fluid inclusions at different depths in the Sanshandao gold deposit, Jiaodong Peninsula, China. *Geofluids* **2013**, *13*, 528–541. [\[CrossRef\]](#)
2. Liu, Y.Z.; Yang, L.Q.; Wang, S.R.; Liu, X.D.; Wang, H.; Li, D.P.; Wei, P.F.; Cheng, W.; Chen, B.Y. Origin and Evolution of Ore-Forming Fluid and Gold-Deposition Processes at the Sanshandao Gold Deposit, Jiaodong Peninsula, Eastern China. *Minerals* **2019**, *9*, 189. [\[CrossRef\]](#)
3. Du, Y.H.; Liu, W.T.; Meng, X.X.; Pang, L.F.; Han, M.K. Effect of Crack Propagation on Mining-Induced Delayer Water Inrush Hazard of Hidden Fault. *Geofluids* **2021**, *2021*, 6557578. [\[CrossRef\]](#)
4. Peng, K.; Li, X.B.; Wang, Z.W. Hydrochemical characteristics of groundwater movement and evolution in the Xinli deposit of the Sanshandao gold mine using FCM and PCA methods. *Environ. Earth Sci.* **2015**, *73*, 7873–7888. [\[CrossRef\]](#)
5. He, T.M.; Zhao, Q.; Ha, J.; Xia, K.W.; Grasselli, G. Understanding progressive rock failure and associated seismicity using ultrasonic tomography and numerical simulation. *Tunn. Undergr. Space Technol.* **2018**, *81*, 26–34. [\[CrossRef\]](#)
6. Wang, M.M.; Li, P.; Wu, X.W.; Chen, H.R. A study on the brittleness and progressive failure process of anisotropic shale. *Environ. Earth Sci.* **2016**, *75*, 886. [\[CrossRef\]](#)
7. Xue, L.; Qin, S.Q.; Sun, Q.; Wang, Y.Y.; Lee, L.; Li, W.C. A Study on Crack Damage Stress Thresholds of Different Rock Types Based on Uniaxial Compression Tests. *Rock Mech. Rock Eng.* **2014**, *47*, 1183–1195. [\[CrossRef\]](#)
8. Nicksiar, M.; Martin, C.D. Evaluation of Methods for Determining Crack Initiation in Compression Tests on Low-Porosity Rocks. *Rock Mech. Rock Eng.* **2012**, *45*, 607–617. [\[CrossRef\]](#)
9. Li, C.B.; Xie, H.P.; Wang, J. Anisotropic characteristics of crack initiation and crack damage thresholds for shale. *Int. J. Rock Mech. Min. Sci.* **2020**, *126*, 104178. [\[CrossRef\]](#)

10. Wei, L.; Liu, Q.; Liu, X. An Improved Crack Initiation Stress Criterion for Brittle Rocks under Confining Stress. *IOP Conf. Ser. Earth Environ. Sci.* **2018**, *170*, 22141. [[CrossRef](#)]
11. Xiao, W.; Zhang, D.; Wang, X. Experimental study on progressive failure process and permeability characteristics of red sandstone under seepage pressure. *Eng. Geol.* **2020**, *265*, 105406. [[CrossRef](#)]
12. Amann, F.; Button, E.A.; Evans, K.F.; Gischig, V.S.; Blümel, M. Experimental Study of the Brittle Behavior of Clay shale in Rapid Unconfined Compression. *Rock Mech. Rock Eng.* **2011**, *44*, 415–430. [[CrossRef](#)]
13. Song, Z.; Zhang, J. Research on the progressive failure process and fracture mechanism of rocks with the structural evolution perspective. *J. Struct. Geol.* **2022**, *154*, 104484. [[CrossRef](#)]
14. Luo, Y.; Gong, H.; Xu, K.; Pei, C.; Wei, X.; Li, X. Progressive failure characteristics and energy accumulation of granite with a pre-fabricated fracture during conventional triaxial loading. *Theor. Appl. Fract. Mech.* **2022**, *118*, 103219. [[CrossRef](#)]
15. Yan, B.Q.; Tannant, D.D.; Ren, F.H.; Cai, M.F. Effects of Silica Fume on the Performance of Cemented Paste Backfill Mixed with Brine. *Geotech. Geol. Eng.* **2019**, *37*, 4575–4587. [[CrossRef](#)]
16. Jia, C.J.; Xu, W.Y.; Wang, H.L.; Wang, R.B.; Yu, J.; Yan, L. Stress dependent permeability and porosity of low-permeability rock. *J. Cent. South Univ.* **2017**, *24*, 2396–2405. [[CrossRef](#)]
17. Chen, Y.; Hu, S.; Wei, K.; Hu, R.; Zhou, C.; Jing, L. Experimental characterization and micromechanical modeling of damage-induced permeability variation in Beishan granite. *Int. J. Rock Mech. Min. Sci.* **2014**, *71*, 64–76. [[CrossRef](#)]
18. Wang, Z.H.; Ren, W.G.; Tan, Y.L.; Konietzky, H. Experimental and Numerical Study on Hydromechanical Coupled Deformation Behavior of Beishan Granite considering Permeability Evolution. *Geofluids* **2020**, *2020*, 8855439. [[CrossRef](#)]
19. Souley, M.; Homand, F.; Pepa, S.; Hoxha, D. Damage-induced permeability changes in granite: A case example at the URL in Canada. *Int. J. Rock Mech. Min. Sci.* **2001**, *38*, 297–310. [[CrossRef](#)]
20. Oda, M.; Takemura, T.; Aoki, T. Damage growth and permeability change in triaxial compression tests of Inada granite. *Mech. Mater.* **2002**, *34*, 313–331. [[CrossRef](#)]
21. Wang, S.; Elsworth, D.; Liu, J. Permeability evolution during progressive deformation of intact coal and implications for instability in underground coal seams. *Int. J. Rock Mech. Min. Sci.* **2013**, *58*, 34–45. [[CrossRef](#)]
22. Chen, Y.; Wei, K.; Liu, W.; Hu, S.; Hu, R.; Zhou, C. Experimental Characterization and Micromechanical Modelling of Anisotropic Slaters. *Rock Mech. Rock Eng.* **2016**, *49*, 3541–3557. [[CrossRef](#)]
23. Hu, Z.; Klaver, J.; Schmatz, J.; Dewanckele, J.; Littke, R.; Krooss, B.M.; Amann-Hildenbrand, A. Stress sensitivity of porosity and permeability of Cobourg limestone. *Eng. Geol.* **2020**, *273*, 105632. [[CrossRef](#)]
24. Meng, T.; Liu, R.; Meng, X.; Zhang, D.; Hu, Y. Evolution of the permeability and pore structure of transversely isotropic calcareous sediments subjected to triaxial pressure and high temperature. *Eng. Geol.* **2019**, *253*, 27–35. [[CrossRef](#)]
25. Zhao, C.X.; Liu, J.F.; Lyu, C.; Xu, D.; Liang, C.; Li, Z.C. Investigation on the mechanical behavior, permeability and failure modes of limestone rock under stress-seepage coupling. *Eng. Fail. Anal.* **2022**, *140*, 106544. [[CrossRef](#)]
26. Zhang, M.; Takahashi, M.; Morin, R.H.; Esaki, T. Evaluation and application of the transient-pulse technique for determining the hydraulic properties of low-permeability rocks—Part 2: Experimental application. *Geotech. Test. J.* **2000**, *23*, 91–99.
27. Li, S.; Li, Y.; Li, Y.; Wu, Z.; Zhou, G. Permeability-strain equations corresponding to the complete stress—Strain path of Yin Zhuang Sandstone. *Int. J. Rock Mech. Min. Sci. Geomech. Abstr.* **1994**, *31*, 383–391.
28. Selvadurai, A.; Boulon, M.J.; Nguyen, T.S. The permeability of an intact granite. *Pure Appl. Geophys.* **2005**, *162*, 373–407. [[CrossRef](#)]
29. Wen, D.S.; Wang, X.Z.; Ding, H.Z.; Fu, Z.B. Estimation of Crack Initiation Stress Based on Axial Crack Strain Expansion Rate. *Rock Mech. Rock Eng.* **2023**, *56*, 1025–1041. [[CrossRef](#)]
30. Eberhardt, E.; Stead, D.; Stimpson, B. Quantifying progressive pre-peak brittle fracture damage in rock during uniaxial compression. *Int. J. Rock Mech. Min. Sci.* **1999**, *36*, 361–380. [[CrossRef](#)]
31. Davarpanah, M.; Somodi, G.; Kovács, L.; Vásárhelyi, B. Complex analysis of uniaxial compressive tests of the Moragy granitic rock formation (Hungary). *Stud. Geotech. Mech.* **2019**, *41*, 21–32. [[CrossRef](#)]
32. Si, X.F.; Li, X.B.; Gong, F.Q.; Huang, L.Q.; Ma, C.D. Experimental investigation on rockburst process and characteristics of a circular opening in layered rock under three-dimensional stress conditions. *Tunn. Undergr. Space Technol.* **2022**, *127*, 104603. [[CrossRef](#)]
33. Tang, M.H.; Wang, G.B.; Chen, S.W.; Yang, C.H. An Objective Crack Initiation Stress Identification Method for Brittle Rock Under Compression Using a Reference Line. *Rock Mech. Rock Eng.* **2021**, *54*, 4283–4298. [[CrossRef](#)]
34. Chen, M.; Liu, J.; Xie, Z.Y.; Liu, J.J.; Hu, X.J.; Li, B.Y.; Cen, Y. Discrete Element Modeling on Mechanical Behavior of Heterogeneous Rock Containing X-Shaped Fissure under Uniaxial Compression. *Geofluids* **2020**, *2020*, 8828199. [[CrossRef](#)]
35. Zhao, X.L.; Zhou, T.; Zhai, T.Q.; Ju, Y.; Zhu, J.B. Experimental investigation on crack initiation and damage stresses of deep granite under triaxial compression using acoustic methods. *J. Rock Mech. Geotech. Eng.* **2023**, *15*, 3071–3078. [[CrossRef](#)]
36. Liu, G.; Sun, W.C.; Lowinger, S.M.; Zhang, Z.H.; Huang, M.; Peng, J. Coupled flow network and discrete element modeling of injection-induced crack propagation and coalescence in brittle rock. *Acta Geotech.* **2019**, *14*, 843–868. [[CrossRef](#)]
37. Yang, T.J.; Wang, P.Y.; Wang, S.H.; Liu, H.; Zhang, Z. Experimental Study on Shear-Seepage Coupling Characteristics of Single Fractured Rock Mass Under Cyclic Loading and Unloading. *Rock Mech. Rock Eng.* **2023**, *56*, 2137–2156. [[CrossRef](#)]
38. Zheng, Z.; Xu, H.; Wang, W.; Mei, G.; Liu, Z.; Zheng, H.; Huang, S. Hydro-mechanical coupling characteristics and damage constitutive model of low-permeability granite under triaxial compression. *Int. J. Damage Mech.* **2022**, *32*, 235–261. [[CrossRef](#)]

39. Passelègue, F.X.; Brantut, N.; Mitchell, T.M. Fault Reactivation by Fluid Injection: Controls from Stress State and Injection Rate. *Geophys. Res. Lett.* **2018**, *45*, 12837–12846. [[CrossRef](#)]
40. Zhang, Q.; Li, X.C.; Bai, B.; Hu, S.B.; Shi, L. Effect of Pore Fluid Pressure on the Normal Deformation of a Matched Granite Joint. *Processes* **2018**, *6*, 107. [[CrossRef](#)]
41. Wang, G.C.; Liu, Y.Y.; Liu, K.; Xu, C.T. Dynamic response and liquefaction potential of porous seabed induced by partial standing ocean waves. *Sci. Rep.* **2023**, *13*, 19061. [[CrossRef](#)] [[PubMed](#)]
42. Wang, J.L.; Ma, B.J.; Zhao, L.X.; Su, P.B.; Wu, S.G. Rock physics diagnostics to characterize early diagenetic processes in hemipelagic calcareous ooze in the northern South China Sea margin. *Mar. Geophys. Res.* **2023**, *44*, 20. [[CrossRef](#)]
43. Zain-Ul-Abidin, M.; Henk, A. Thermal-Hydraulic-Mechanical (THM) Modelling of Short-Term Gas Storage in a Depleted Gas Reservoir—A Case Study from South Germany. *Energies* **2023**, *16*, 3389. [[CrossRef](#)]
44. Mun, W.; McCartney, J.S. Compression mechanisms of unsaturated clay under high stresses. *Can. Geotech. J.* **2015**, *52*, 2099–2112. [[CrossRef](#)]
45. Chen, S.; Zhao, Z.; Chen, Y.; Yang, Q. On the effective stress coefficient of saturated fractured rocks. *Comput. Geotech.* **2020**, *123*, 103564. [[CrossRef](#)]
46. Civan, F. Drilling Mud Filtrate and Solids Invasion and Mudcake Formation. *Reserv. Form. Damage* **2007**, 741–774. [[CrossRef](#)]
47. Ghabezloo, S.; Sulem, J.; Guédon, S.; Martineau, F. Effective stress law for the permeability of a limestone. *Int. J. Rock Mech. Min. Sci.* **2009**, *46*, 297–306. [[CrossRef](#)]
48. Meng, F.; Li, X.; Baud, P.; Wong, T. Bedding anisotropy and effective stress law for the permeability and deformation of clayey sandstones. *Rock Mech. Rock Eng.* **2021**, *54*, 5167–5184. [[CrossRef](#)]
49. Xiao, W.; Li, T.; Li, M.; Zhao, J.; Zheng, L.; Li, L. Evaluation of the stress sensitivity in tight reservoirs. *Petroleum Explor. Dev.* **2016**, *43*, 115–123. [[CrossRef](#)]
50. Walsh, J.B. *Effect of Pore Pressure and Confining Pressure on Fracture Permeability*; Elsevier: Amsterdam, The Netherlands, 1981.
51. Zhang, X.; Wu, C.; Wang, Z. Experimental study of the effective stress coefficient for coal permeability with different water saturations. *J. Pet. Sci. Eng.* **2019**, *182*, 106282. [[CrossRef](#)]

**Disclaimer/Publisher’s Note:** The statements, opinions and data contained in all publications are solely those of the individual author(s) and contributor(s) and not of MDPI and/or the editor(s). MDPI and/or the editor(s) disclaim responsibility for any injury to people or property resulting from any ideas, methods, instructions or products referred to in the content.